Effects of free-stream turbulence on high pressure turbine blade heat transfer predicted by structured and unstructured LES

E. Collado Morata[a,1], N. Gourdain[b], F. Duchaine[b], L.Y.M. Gicquel[b]

[a]*TURBOMECA, ave. J. Szydlowski, 64510 Bordes, France*
[b]*CERFACS, 42 ave. G. Coriolis, 31057 Toulouse, France*

Abstract

Recent developments and demonstrations for the prediction of turbulent flows around blades point to Large Eddy Simulations (LES) as a very promising tool. Indeed and despite the fact that this numerical method still requires modeling and intense computing effort compared to Reynolds Average Navier Stokes (RANS), this fully unsteady simulation technique provides valuable information on the turbulent flow otherwise inaccessible. Theoretical limits and scales of wall bounded flows are now well mastered in simple cases but complex industrial applications usually introduce unknowns and mechanisms that are difficult to apprehend beforehand especially with LES which is usually computationally intensive and bounded to code scalability, mesh quality, modeling performances and computer power. In this specific context, few studies directly address the use of fully structured versus unstructured, implicit versus explicit flow solvers and their respective impact for LES modeling of complex wall bounded flows. To partly address these important issues, two dedicated structured and unstructured computational solvers are applied and assessed by comparing the predictions of the heat transfer around the experimental high pressure turbine blade profile cascade of Arts et al. (1990). First, both LES predictions are compared to RANS modeling with a particular interest for the accuracy/cost ratio and improvement of the physical phenomena around the blade. LES's are then detailed and further investigated to assess their ability to reproduce the inlet turbulence effect on heat transfer and the development of the transitioning boundary layer around the blade. Quantitative comparisons against experimental findings show excellent agreement especially on the pressure side of the profile. Detailed analysis of the flow predictions provided by both the structured and unstructured solvers underline the importance of long stream-wise streaky structures responsible for the augmentation of the heat transfer and leading to the transition of the suction-side boundary layer.

Keywords: Turbine guide vane, LES, Unsteady flow, Heat transfer, Boundary layer transition

Email address: collado@cerfacs.fr (E. Collado Morata)
[1]Tel:+33 (0)5 61 19 31 22; fax:+33 (0)5 61 19 30 00

1. Introduction

Most industrial energy or propulsion systems differentiate themselves in the technological solutions devised at the development stage to manage the notion of thermal efficiency of the machines. Although common to both applications, ensuring efficient machines with optimal thermodynamical cycles, that is to say minimum losses, is still a very difficult task that requires accurate design tools and rules which cover different physics [33]. Indeed not only should one master flows yielding minimum pressure drop but also radiative, conduction and convection heat transfers [3, 5]. The latter problem is directly linked to flow analyses and is particularly difficult since to be predictive one needs to address complex interactions taking place at the flow boundaries or more specifically in the near wall region. Flow physics at walls is a recurrent challenge and is still an open problem that covers laminar to turbulent, natural and forced transitions, compressibility effects such as shocks, wall curvature or roughness, Free-Stream Turbulence (FST) intensity, external pressure gradient effects, etc [4, 14]. In industrial applications, such issues and difficulties also point to massively separated flows, reattachment points, rotational forces, re-laminarization, etc. In the context of gas turbine applications, thermal management becomes critical for the high pressure turbine located directly after the combustion chamber and which experiences high temperature gradients at walls. Typical engine life duration today directly relies on the capacity of designers to correctly estimate the impact of unsteady hot streaks generated by the burner flow as well as the wall heat transfer at the blade wall [24]. Unfortunately, such flow phenomena are extremely difficult to predict in such aggressive environment where technological small scale devices (such as cooling holes, tip gap, etc.) impact the turbine flows and clearly increase geometrical complexity. Finally, turbulence also plays a major role on heat transfer and a laminar to turbulent transition is often observed on the turbine blade walls.

Despite such long-lived difficulties, classical steady state Computational Fluid Dynamics (CFD) simulations are the only alternative to correlations for most gas turbine configurations [42]. Conjugate heat transfer with weak coupling is also used and partly validated in such context [17]. These CFD solutions are indeed very attractive as they induce relatively short response time in comparison to more costly experimental campaigns. However the validation of CFD codes requires important features like well documented test cases, accurate numerical schemes, grid flexibility and validated turbulence or transition modeling/simulations [30, 60]. From a purely numerical point of view, a large range of numerical methods is nowadays available in the literature, all of which are more or less suited to near wall flows [25, 37, 52, 53, 61, 63]. RANS simulations require all the turbulent scales of the flow to be modeled putting stringent modeling effort on the turbulent closures near walls [1, 30, 40, 58]. RANS simulations however inherit from years of research and developments. The limits and advantages of RANS simulations are known and it is routinely used in the design phase of most industrial applications. Fully unsteady numerical methods where all turbulent scales (Direct Numerical Simulations, DNS) or parts of the scales (LES) are solved for are also available. Although the former is clearly out of reach for real applications, the latter still requires to prove its efficiency. Recent contributions based on LES [53, 54] provide promising results especially for the prediction of heat transfer in fundamental test cases [7, 68] or complex geometry [8, 17].

One critical aspect that further complexifies the use of LES for blade heat transfer predictions, is the sensitivity of the procedure to modeling which is usually linked to the local grid resolution, numerics and cell topology. Theoretically well defined isotropic and uniform meshes are better suited for LES. Near walls structured meshes comply to the preferred directions of such flows and ease the use and development of high order numerical schemes with low dispersion and dissipation properties to ensure that the Sub-Grid Scale (SGS) model works adequately and as designed [47]. Many turbine CFD investigations hence consider structured grids [10]. This method suffers, however, a major drawback: the difficulty to refine localized regions that also need to comply with the meshing of technological devices. A potential answer is the use of unstructured grids that represent a promising way for local mesh refinements necessary to take into account very complex geometries (cooling holes, etc.) [17, 32]. Very few contributions directly discuss the use of structured or unstructured LES solvers for blade flows [35] and one intent of this contribution is to address this issue. To do so, the comparison of LES and RANS predictions is first proposed to emphasize the differences of the two approaches for a test case representative of turbine flows: the first stage of an uncooled, transonic, high-pressure turbine [6]. Comparisons of LES predictions obtained using a fully structured solver and a fully unstructured one are detailed and compared to experiments. Irrespectively of the solver used clear common features are recovered and in good agreement with experimental data. Typically, for the investigated operating point, observations show a by-passed transition on the blade suction side, which is very difficult to predict with conventional numerical flow solvers. Experimental data [6] also indicates that the solution is largely dependent on the external turbulence level, a sensitivity which is confirmed and captured by the two LES approaches.

The paper is arranged as follows. The experimental target configuration is first introduced in Section 2 along with the dependency to the upstream FST intensity of the experiment and its length scale. Section 3 provides the description of the numerical methods, models, computational domains, meshes and sets of boundary conditions used for CFD. The first part of Section 4 is devoted to the analysis of the results with first comparisons against experimental findings of structured RANS and LES predictions. Structured versus unstructured LES is detailed in Subsection 4.1.1 and 4.1.2 for aerothermal prediction with and without FST, respectively. Subsection 4.2.1 is dedicated to the sensitivity of the calculations to geometric parameters and the potential impact it may have on heat transfer predictions. In the last part of Section 4, the ability of LES to reproduce the sensitivity of the flow to FST is illustrated. For this specific analysis, different values of FST are investigated and specific flow structures are studied, before concluding by Section 5.

2. Reference experimental setup and conditions

The context of application of this study is the qualification of LES for the improvement of heat transfer predictions around distributor blades located right at the exit of the combustion chamber of aeronautical gas turbine engines. This specificity imposes having access to a high Mach number flow facility with detailed data around blades typical of turbines. To meet this purpose the VKI LS 89 case [6] is retained since it is constructed to specifically address and

validate CFD methods and exhibit many of the fine mechanisms often present in real applications.

2.1. The LS89 case

The tested configuration is a $2D$ turbine blade cascade, called LS 89 blade, largely described in Arts et al. [6] and displayed in Fig. 1. Only the central passage is investigated and aims at simulating a blade to correspond to periodic flow conditions. The blade chord C is of 67.647 mm with a pitch/chord ratio of 0.85 and is placed at an angle of attack of $0°$.
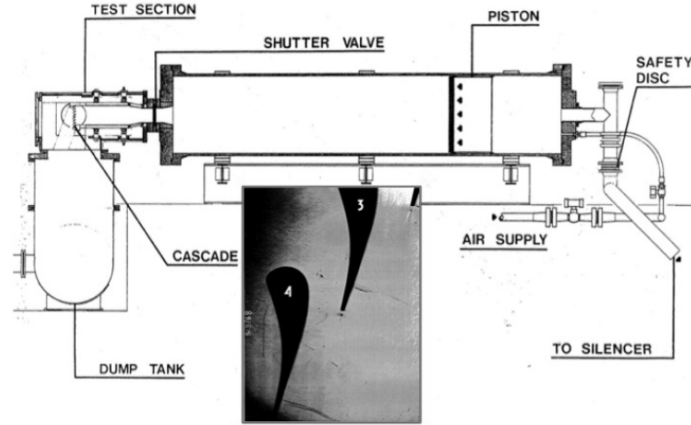

Figure 1: Experimental facility investigated by Arts et al. (1990) [6].

The convective heat transfer coefficient, H, measured in this experimental rig is defined as the ratio between the wall heat flux, q_{wall}, and the difference between the total free stream temperature, T_0 and the local wall temperature, T_{wall}, Eq. (1).

$$H = \frac{q_{wall}}{T_0 - T_{wall}} \tag{1}$$

Test case	Re_2	$M_{is,2}$	$P_{i,0}$	$T_{s,wall}$	Tu_0
MUR129	$1.13\,10^6$	0.840	$1.87\,10^5$ Pa	298 K	1.0%
MUR235	$1.15\,10^6$	0.927	$1.85\,10^5$ Pa	301 K	6.0%

Table 1: Test cases and details of the flow conditions for VKI experiment.

A large range of free stream conditions have been experimentally investigated but only two configurations are explored in this work, Table. 1, where the indices 0 and 2 denote quantities at the inlet and outlet, respectively. The adjustment of the position of the turbulence grid relative to the cascade controls the variation of the turbulence intensity. The considered Reynolds numbers, Re_2, based on the chord and outlet velocity is approximately equal to

10^6 for both cases while the inlet FST intensity, Tu_0, equals 1% and 6% respectively. This two-set configuration is believed to be the more representative conditions present in a real turbine. Both cases have approximately the same inlet total pressure, $P_{i,0}$ and static mean wall temperature, $T_{s,wall}$. The isentropic Mach number at the outlet is slightly different between the cases ($M_{is,2}$=0.840 and 0.927).

The flow topology expected around the airfoil is represented schematically in Fig. 2. Several phenomena can be determined for the LS89 case: (1) is the well-know Von Karman vortex shedding in the blade's wake. This vortex shedding creates pressure waves emitted from the unsteady boundary layer detachment at the trailing edge. These pressure waves (2) then travel upstream and downstream the flow interacting with other flow regions. Part of the impacting pressure waves on the suction side wall of the underneath blade, (3), is reflected back into the main channel. Skin vortices (4) can also be created from this impact and will then interact with the flow on the suction side. Note also that the downstream propagating pressure wave also interacts with the wake structures. With the operating conditions targeted, a shock wave, (5), could be present with appearance of supersonic regions. These complex flow phenomena have to be taken into account since they affect the aerodynamic field around the blade, and therefore, the heat transfer, which is one of the quantities of interest to turbine designers. An additional difficulty with these conditions is evidenced by the dependency of the flow patterns to the upstream turbulence as further discussed below and illustrated in Fig. 6.
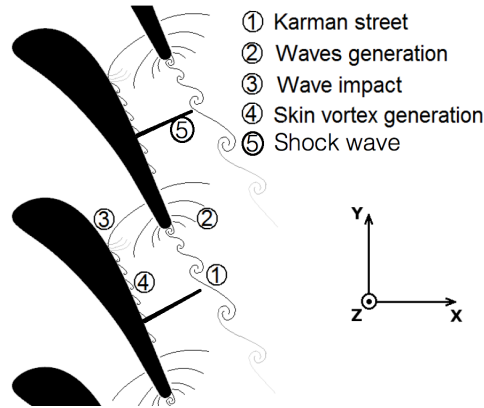

Figure 2: Schematic view of the flow topology around the LS89 blade (based on the MUR235 case).

2.2. Dependency to the upstream veine turbulence

In the last decades, the effect of FST and its length scale has been largely studied experimentally in high turbine passages. Yardi et al.[66] analyzed those effects on the stagnation regions of a cylinder concluding that the maximum effects appear for a dimensionless length scale $L/D\sqrt{Re_D}$ between 5 and 15, where L is the integral length scale of the turbulence and D is the cylinder diameter. Dullenkopf and Mayle [19] found that fluctuations at low frequencies only impact the quasi-steady state, while those of high frequencies are damped by viscosity. As a result, only a narrow

band of the turbulence intensity has an influence on heat transfer. Their major conclusion is that the augmentation of heat transfer varies linearly with the intensity weighted by the effective length scale. Ames et al.[4] analyzed the transition location with respect to the FST intensity and length scale in a C3X blade cascade. In the experiment, the decrease of the length scale increases the heat transfer and the transition location moves towards the leading edge when intensifying the turbulence intensity.

Pressure gradient and surface curvature play also a major role on the flow structure and the boundary layer response, which ultimately controls the heat transfer. As seen in Fig. 3, where experimental results from Table 1 are plotted, the heat transfer can be increased by 40% on the pressure side if turbulence is present in the main stream. Görtler observes that the boundary layer on a concave surface becomes unstable under the effect of centrifugal forces [21]. Stream-wise vortices appear along the wall, known as Görtler vortices, which are responsible of an increased local vorticity and enhanced heat transfer to the blade. Unsteady vortical structures are detected also at the leading edge in the LES of Xiong et al. [65]. On the suction side, Fig. 3 underlines that the transition onset is different for the experiment with and without FST. This particular point will be largely discussed in Subsection 4.2.2.
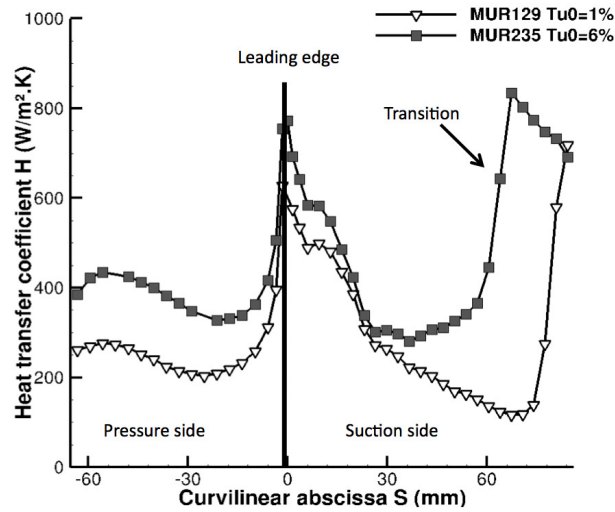

Figure 3: Experimental profiles of the local heat transfer coefficient, H, as a function of the blade curvilinear abscissa S (negative values for the pressure side and positive values for the suction side of the blade, the zero corresponding to the leading edge position) and Tu_0, inlet FST intensity, results from Arts et al. [6].

As the FST intensity is known in the experiment, the reader would expect a comparison of the Power Spectrum Density (PSD) between the experiment and the simulations. Results extracted at the leading edge location can serve as a validation of inlet turbulent conditions. However, there is no information in the experiments reported by Arts et al. [6] about the PSD at the considered turbulent intensities. The second point is that the length scale of inlet turbulence, L_0, is not known. To better deal with this problem, a parametric study has been added in the Subsection

6

4.2.2 to show the effect of the turbulent length scale on the wall heat transfer.

Numerically, the principal limits of RANS simulations are the accurate prediction of the transition onset: traditional turbulence models predict a fully turbulent flow while in reality there is a transition zone. Significant improvements have been achieved in RANS based transition models [38]. For LES, while profuse in low pressure turbine [44, 64], numerical analysis on high pressure turbine have not been addressed, except by Bhaskaran et al. [8].

3. Numerical simulations

Irrespectively of the turbulent modeling formalism adopted for the computation (*i.e.*, RANS or LES), the initial governing equations are the unsteady compressible Navier-Stokes equations that describe the conservation of mass, momentum and energy. In conservative form, it can be expressed in three-dimensional coordinates as:

$$\frac{\partial \mathbf{W}}{\partial t} + div\,\mathbf{F} = 0 \tag{2}$$

where $\mathbf{W}$ in Eq. (2) is the vector of primary variables themselves function of time, t and space, $\mathbf{x}$. $\mathbf{F} = (\mathbf{f} - \mathbf{f_v}, \mathbf{g} - \mathbf{g_v}, \mathbf{h} - \mathbf{h_v})$ is the flux tensor; $\mathbf{f}, \mathbf{g}, \mathbf{h}$ are the inviscid fluxes and $\mathbf{f_v}, \mathbf{g_v}, \mathbf{h_v}$ are the viscous fluxes (including the potential contribution of models for turbulence through the addition of the so-called turbulent viscosity, ν_t). The fluid follows the ideal gas law $p = \rho\, r\, T$, where r is the mixture gas constant, T, the temperature and ρ, the density. The fluid viscosity follows Sutherland's law and the heat flux follows Fourier's law.

3.1. Turbulence modeling for RANS and LES

The high Reynolds number related to the studied flow implies that all the flow scales can not be efficiently represented directly with current grid sizes. Turbulence modeling is thus necessary to allow computing such flows. Different formalisms exist and the most common approach for complex configurations is still RANS which proposes to model the effect of all the turbulent scales on the mean flow in statistically stationary cases. For this formalism, the mathematical operation introduced relies on the statistical ensemble of independent realizations of the same flow problem from which only the statistical ensemble means are of interest. The initial system of equations is thus usually supplemented by additional modeled transport equations to specifically address turbulence local non-equilibrium or other turbulent flow features [37, 52, 61, 63]. With this approach and for the specific problem of the boundary layer transition, transition criteria [1, 30, 40, 58] can be added. Note that this modeling formalism has been applied to turbine flows with moderate success [36, 39]: the transition criteria are effective to match the experiments (if the solution is known) but they usually suffer from a lack of universality.

A more comprehensive method and particularly less demanding modeling formalism is obtained with LES. In this approach the notion of separation of turbulent scales is introduced and distinguishes a separation between the resolved (large) turbulent scales and the modeled (small) scales [20, 45, 50, 52, 53]. This separation of scales is obtained by filtering out the small flow scales that can not be properly represented by the mesh, their effects on the filtered field

7

being modeled by the so-called SGS model. For compressible LES and RANS, the spatial Favre filtering or ensemble means are used and the operation reduces for spatially, temporally invariant and localized filter functions to:

$$\overline{\rho}\,\widetilde{f} = \begin{cases} \text{RANS:} & \dfrac{1}{N}\displaystyle\sum_{1}^{N}\rho^n(\mathbf{x},t)\,f^n(\mathbf{x},t), \\[2mm] \text{LES:} & \displaystyle\int \rho(\mathbf{x}',t)\,f(\mathbf{x}',t)\,G(\mathbf{x}'-\mathbf{x})\,d\mathbf{x}', \end{cases} \tag{3}$$

where G denotes the filter function while n is the nth realization of a statistical ensemble composed of N of such fields. The unresolved SGS stress tensor $\overline{\tau_{ij}}^t$ and the equivalent Reynolds stress tensor appearing in RANS are usually modeled using the Boussinesq assumption [57]:

$$\overline{\tau_{ij}}^t - \frac{1}{3}\,\overline{\tau_{kk}}^t\,\delta_{ij} = -2\,\overline{\rho}\,\nu_t\,\widetilde{S}_{ij}\,, \tag{4}$$

$$\text{with } \widetilde{S}_{ij} = \frac{1}{2}\left(\frac{\partial\widetilde{u}_i}{\partial x_j}+\frac{\partial\widetilde{u}_j}{\partial x_i}\right) - \frac{1}{3}\,\frac{\partial\widetilde{u}_k}{\partial x_k}\,\delta_{ij}. \tag{5}$$

In Eq. (4), $\widetilde{S}_{ij}$ is the resolved or ensemble mean strain rate tensor and ν_t is the SGS or RANS turbulent viscosity. The unclosed energy flux $\overline{q_i}^t$ is modeled using a turbulent heat conductivity obtained from ν_t by $\lambda_t = \overline{\rho}\,\nu_t\,\overline{c_p}/Pr_t$ where Pr_t is a constant turbulent Prandtl number,

$$\overline{q_i}^t = -\lambda_t\,\frac{\partial\widetilde{T}}{\partial x_i}. \tag{6}$$

In Eq. (6), $\widetilde{T}$ is the Favre filtered temperature which satisfies the modified filtered state equation $\overline{p} = \overline{\rho}\,r\,\widetilde{T}$ [46].

3.1.1. RANS closures:

For this work a two-equations type of closure is adopted. To handle transition, the standard Abu-Ghannam model [1] introduces the intermittency factor γ (parameter representing the time in which the flow is turbulent) but results [22] underline the poor predictive capability of such approaches when there is an impact of FST on the heat transfer around the blade. An improvement, detailed in Section 4.1, is noticed when implementing Menter γ-Re_θ model [43] coupled with a two equation turbulence model k-ω using a correction on the Shear Stress Transport (SST) [42]. The novelty of this correlation-based transition model is not only to use local variables but also their gradients. Such new closure however requires additional transport equations. A transport equation for the intermittency γ model is needed to turn on the production term of the turbulent kinetic energy downstream of the transition point, Eq. (7), where S_γ represents the transition sources.

$$\frac{\partial(\rho\gamma)}{\partial t} + \frac{\partial(\rho U_j\gamma)}{\partial x_j} = S_\gamma + \frac{\partial[(\mu+\frac{\mu_t}{\sigma_f})\frac{\partial\gamma}{\partial x_j}]}{\partial x_j}. \tag{7}$$

A second transport equation is solved in terms of the transition onset momentum-thickness Reynolds number ($\widetilde{Re_{\theta t}}$) and given by Eq. (8). In this equation, $S_{\theta t}$ stands for the source term which forces the transported scalar to match the local value of $Re_{\theta t}$ calculated from an empirical correlation outside the boundary layer. More information of this methodology can be found in Menter et al. [43].

8

$$\frac{\partial(\rho\widetilde{Re}_{\theta t})}{\partial t} + \frac{\partial(\rho U_j\widetilde{Re}_{\theta t})}{\partial x_j} = S_{\theta t} + \frac{\partial[(\mu + \mu_t)\sigma_{\theta t}\frac{\partial\widetilde{Re}_{\theta t}}{\partial x_j}]}{\partial x_j}. \tag{8}$$

3.1.2. LES closures:

The SGS model, used for both structured and unstructured meshes, is the Wall-Adapting Local Eddy-Viscosity (WALE) model [47], specially built to compute turbulence near walls. Similarly to the Smagorinsky model [57], local flow features are lost and only global quantities are represented by the SGS model. Following this closure, the SGS viscosity reads,

$$\nu_t = (C_w\Delta)^2\frac{(s_{ij}^d s_{ij}^d)^{3/2}}{(\tilde{S}_{ij}\tilde{S}_{ij})^{5/2} + (s_{ij}^d s_{ij}^d)^{5/4}}, \tag{9}$$

$$s_{ij}^d = \frac{1}{2}(\tilde{g}_{ij}^2 + \tilde{g}_{ji}^2) - \frac{1}{3}\tilde{g}_{kk}^2\delta_{ij}, \tag{10}$$

In Eq. (9) and Eq. (10) , Δ stands for the filter length ($\propto$ the cubic-root of the cell volume), C_w is the model constant equal to 0.4929 and $\tilde{g}_{ij}$ is the resolved velocity gradient. For the SGS energy flux, $\bar{q}_i{}^t$, Eq. (6), the turbulent Prandtl number coincides with the SGS quantity and differs from the conventional turbulent Prandtl number. The value chosen for the turbulent SGS Prandtl number is 0.6 for both solvers.

3.2. Numerical solvers

Two different solvers are used in this work. The first solver (*elsA*) is specialized in external and internal flow predictions using RANS, LES and DES. It is fully compressible and relies on a temporal implicit marching scheme. The second solver (AVBP) targets reactive flow predictions by use of LES and relies on an explicit temporal integration scheme of the fully compressible multi-species system of equations. Specificities about the numerics adopted for both codes are detailed below for the first code followed by the second code.

The parallel *elsA* software uses a cell centered approach on structured multi-block meshes. More information about this flow solver can be found in Cambier et al. [12]. For (steady-state) RANS simulations, convective fluxes are computed with a second order centered scheme with classical artificial dissipation parameters k^2 and k^4 [27]. Diffusive fluxes are computed with a second-order centered scheme. The pseudo time-marching is performed by use of an efficient implicit time integration approach, based on the backward Euler scheme and a scalar Lower-Upper (LU) Symmetric Successive Over-Relaxation (SSOR) method [67]. As previously indicated, for RANS, the γ-Re_θ Menter model [43] is used coupled with a two-equation k-ω turbulence model with a SST correction [42]. For LES, convective fluxes are computed with a fourth order centered scheme, considering minimal artificial dissipation [18]. The time-marching scheme is based on a second order Dual Time Stepping method [26]. Such implicit algorithms are very attractive to reduce the computational cost since the simulation is stable even with CFL numbers greater than 100 (although clear care is needed and such large values are to be avoided for LES). In the present case, 16, 000 time

steps ($\Delta t = 0.12\mu$s) are necessary to describe one through-flow time (the time for a particle dropped at the inlet to reach the outlet, *i.e.* ≈ 2.0 ms).

The parallel LES code, AVBP [41, 56], solves the full compressible Navier-Stokes equations using a two-step time-explicit Taylor-Galerkin scheme (TTG4A) for the hyperbolic terms on a cell-vertex formulation [15], along with a second order Galerkin scheme for diffusion [16]. TTG4A provides high spectral resolution and both low numerical dissipation and dispersion, which is particularly adequate for LES [34]. Such numerics are especially designed for LES on hybrid meshes and have been extensively validated in the context of turbulent reacting flow applications [9, 59]. The scheme provides $3rd$ order space and time accuracy [15]. The major drawback of this strategy arises from the explicit nature of the solver whose time step is controlled by the low acoustic CFL number preventing from reducing characteristic cell size below the wall unit scale. Therefore, for aerodynamic applications, where the viscous sub-layer needs to be computed, mesh refinements force small time steps ($\propto 10^{-7}$s or lower, Δt = 1.54 10^{-8}s in this particular case) and a higher computational cost is inferred. In the present case, about $130,000$ time steps are necessary to simulate one flow-through time. Note that despite this clear constraint, the unstructured hybrid approach enables refinement of the mesh in zones of interest by using prisms in the wall region for example.

3.3. Computational setup

3.3.1. Computational domain and mesh generation

The computational domain examined is sketched in Fig. 4 (a) accompanied by a view of probe locations , Fig. 4 (b), used in the analysis of the unsteady features predicted by LES . For the structured mesh, the flow domain is discretized with a multi-block approach, using an O-4H meshing strategy for the guide vane passage. A partial view of the structured mesh used is presented in Fig. 5 (a). In order to limit the dependency of the solution to the inlet/outlet positions, the mesh extends up to $0.7\ C$ upstream the blade leading edge and $1.5\ C$ downstream the vane. Typical grid dimensions are $\sim$650 points in the stream-wise direction with $\sim$780 points around the blade, $\sim$175 points in the pitch-wise direction and $\sim$200 points in the span-wise direction. The total number of grid points for the blade passage is 29.7×10^6 points for structured LES and 35.000 points for 2D RANS. Typical cell sizes in wall units are in agreement with recommended values, suitable for LES predictions [29], Table 2.

For the unstructured simulations, a hybrid approach with prismatic layers at the wall and tetrahedra in the main duct, Fig. 5 (b), is adopted to reduce the number of cells in the nearby region of the wall and to meet the preferential directions of the boundary layer flow. The solution adopted has 5 layers of prisms where the vertical length of the prism Δy is smaller than the triangle base-length Δx or Δz (here, $\Delta x \sim \Delta z$) resulting in a minimum cell volume that is increased if compared to a full tetrahedral option. A limit is imposed to this mesh adaptation to avoid numerical errors in these layers, the aspect ratio of the first and thinnest layer is set to $\Delta x^+ \sim 4\Delta y^+$, *i.e.*, $x^+ \approx 4y^+$ in agreement with known observations and boundary layer scales [11]. The last constraint to control, which is known to be critical numerically, is the stretching ratio. It can be defined as the ratio of the characteristic length of an element of a layer to the characteristic length of the neighboring cell. In this particular case, the characteristic length is equal to the prism
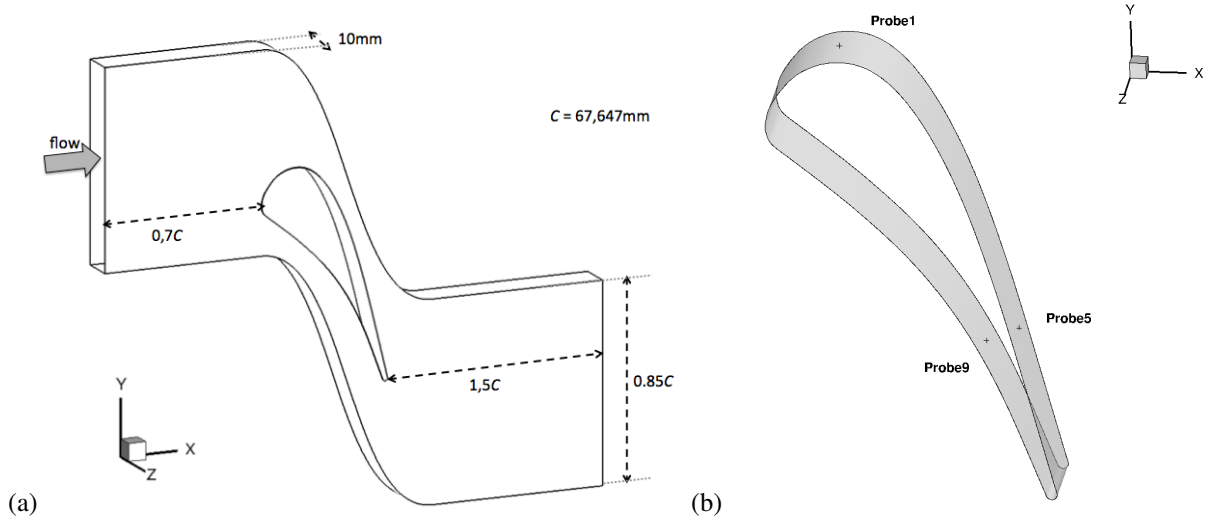
10

Figure 4: (a) Sketch of the computational domain and (b) visualization of three of numerical probes used to diagnose LES predictions.

height. The stretching ratio is here equal to 1.09. Taking into account all the constraints of this strategy, 29.3×10^6 (6.3×10^6 prisms and 23×10^6 tetrahedra) cells are required, Table 2. Typical grid properties are $6,000$ points around the blade, ~ 200 points in the pitch-wise direction and ~ 230 points in the span-wise direction.
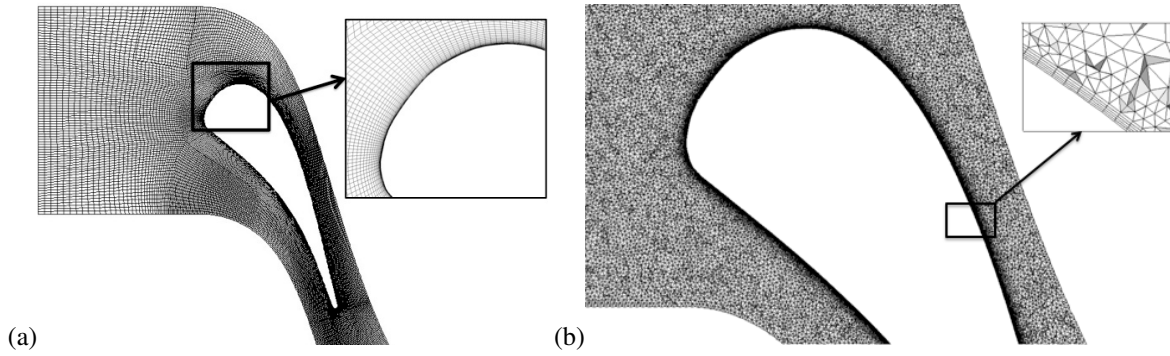
Figure 5: (a) Detail of the structured mesh grid and (b) unstructured mesh grid for the LS89 blade.

Not only regarding mesh size, but also CPU needs is LES much more costly than RANS simulations, by a factor of approximately 6,000 for the meshes of Table 2. The main reasons are of course mesh requirements and formalisms: RANS only costs 0.3 CPU hours (~ 15 CPUh for a full 3D simulation) to reach convergence. The simulation of 10 through-flow times for the structured LES solver requires $90,000$ CPU hours for the same state, Table 3. Note also that 10 through-flow times is the time necessary to converge statistical quantities of the flow. The equivalent cost with

11

	RANS	LES	LES
	structured	structured	unstructured
$< y^+ >$	~ 1	~ 1	~ 4
1st **layer size**	2μm	2μm	8μm
	2D	$\Delta z^+ \sim 25$	$\Delta z^+ \sim 4\Delta y^+$
		$\Delta x^+ \sim 150$	$\Delta x^+ \sim 4\Delta y^+$
Mesh size	0.035M cells	29.7M cells	29.3M cells

Table 2: Wall refinement and mesh size for RANS and LES approaches for MUR235.

the fully unstructured approach yields $140,000$ CPU hours.[2]

	RANS	LES	LES
	structured	structured	unstructured
CFL	20	25	0.9
Time step	NA	$1.2 \ 10^{-7}$s	$1.54 \ 10^{-8}$s
CPU cost	t_{RANS}	$\sim 6000 \ t_{RANS}$	$\sim 1.5{*}6000 \ t_{RANS}$

Table 3: Temporal parameters and CPU cost comparison for all the approaches for MUR235.

3.3.2. Boundary conditions

Inflow and outflow mean conditions are applied for both codes based on available experimental data, Table. 1. Walls are treated as isothermal and the mean static pressure is applied at the downstream end to set the outlet isentropic Mach number at the desired value. Periodicities are used for lateral and radial ("top and bottom") sections of the computational domain, Fig. 4 (a).

Specific attention is taken for the inflow conditions, the difficulty relating to the studied flow imposing to take into account the turbulence intensity. Mean inflow information is first set for all simulations based on measured total temperature and total pressure for both solvers: *i.e.*, the mean carrying field is constant in space and time at the inflow. For RANS simulations, turbulence intensity is of critical importance along with the turbulent length-scale for the transition criterion [43]. There are set constant in time and space at a reference chosen value of the inflow condition (Tu_0=6% and L_0=1.5mm). The main drawback of this modeling, analyzed in Subsection 4.1.2, is that it is not able to take into account the effect of turbulent structures in the suction side of the blade, which are responsible of an increase of 40% in the heat transfer when there is FST.

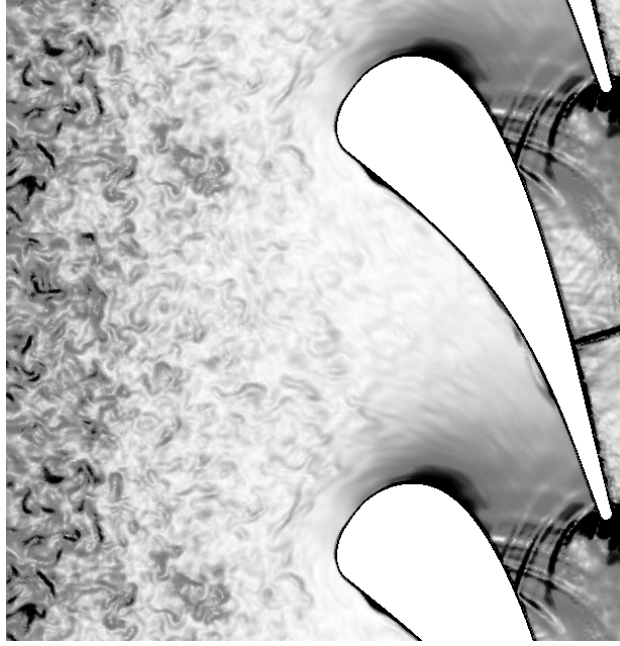[2]All numerical simulations are performed on a SGI Altix computing platform.

Figure 6: Instantaneous field of $||\frac{\partial \rho}{\partial x_i}||/\rho$ as obtained by unstructured LES using synthetic turbulence [31] at the inflow boundary.

For LES, the notion of turbulent inflow imposes a notion of unsteadiness as well as spatial variations of the flow at the inflow condition. Different methods exist either relying on a turbulent channel precursive simulation [8], synthetic turbulence [13] or recycling methods [28]. The aim of all these methods remains common and is to mimic the effects of turbulence without relying on white noise that is not effective due to the lack of spatial and temporal coherence. The methods retained for the study are the "2D" version of the "Synthetic Eddy Method" (SEM) proposed by Jarrin et al. [28] available with the structured LES solver and the synthetic approach proposed by Guezennec et al. [23] for the unstructured solver, Fig. 6. Although slightly different, these two inflow conditions require a value of Tu_0 and a most energetic turbulent length-scale, L_e. They are conceptually identical and yield similar LES results on simple turbulent flows. With both approaches, the inflow information is recast into,

$$\widetilde{u}_i(\mathbf{x},t) = <\widetilde{u}_i>(\mathbf{x}) + \widetilde{u}_i'(\mathbf{x},t) \text{ with } \frac{\partial \widetilde{u}_i'}{\partial x_i} = 0. \tag{11}$$

In Eq. (11), $\widetilde{u}_i$, refers to a LES velocity filtered quantity and $<\widetilde{u}_i>$ refers to the RANS equivalent. Note that this correspondence supposes a statistically stationary and ergodic flow [52, 61]. $\widetilde{u}_i'$ is defined by its position and its amplitude and results from 100 to 1,000 random wave number fields whose individual amplitudes are divergence free and relate to given turbulent synthetic spectra [49, 51] of given integral length-scale that is proportional to L_e [13, 28, 31].

4. Results and Discussions

In order to proceed and qualify both LES solvers on the LS89 problem, several computations are produced, the detail of which is provided in Table. 4. RANS and LES results are first compared, Subsection 4.1, to study the suitability and limits of these approaches. Case Ia & Ib are confronted to Cases IIa & IIb and IIIa & IIIb in terms of aerodynamical and thermal predictions. More detailed analyses of the two LES strategies in terms of the sensitivity of both the mesh topology and the FST parameters is carried out in Subsection 4.2.

	RANS structured	LES structured	LES unstructured
Scheme	Implicit	Implicit	Explicit
Model	k-ω, transition criteria [42]	WALE	WALE
MUR129	**Case Ia**	**Case IIa**	**Case IIIa**
MUR235	**Case Ib**	**Case IIb**	**Case IIIb**

Table 4: Cases analyzed in Section 4.

4.1. RANS versus LES predictions:

A first point of interest of the present investigation is to quantify and qualify the contribution of LES in the context of highly loaded guide vane of turbines. In the following, Figs. 7 & 8 & 9, direct qualitative comparisons of the available RANS model and both LES are produced for the two operating conditions (all Cases from Table.4). For the MUR129 case, all solvers predict a subsonic flow around the blade, Figs. 7 (a) & 8 (a) & 9 (a). For MUR235, mean flow features are clearly captured by both approaches: *i.e.* the existence of the shocks (noted 1 in Figs. 7 (b) & 8 (b) & 9 (b)), the blade wake and the flow acceleration on the suction side issued by the profile strong curvature are present in RANS and LES. Differences essentially appear in the actual extent of the blade wake and the presence of a Von Karman street in the structured and unstructured LES (Figs. 8 & 9). The Von Karman street is however less visible in Fig. 9 with this scaling. Strong pressure waves generated at the trailing edge flow separation are also evidenced by both LES which is not the case in RANS. When FST is imposed at the inlet, MUR235, LES indicate that turbulent flow patterns impact the vane leading edge, leading to the development of vortices on the pressure side, noted 2 in Fig. 8 (b) and also noticeable in Fig. 9 (b).

More quantitative comparisons are provided on Fig. 10. Aerodynamic fields are first judged through the evolution of the isentropic Mach number along the curvilinear abscissa of the blade, S (set equal to zero for the blade leading edge and negative/positive for the pressure side/suction side, respectively). In agreement with the observations from the flow field views given on Figs. 7 - 9, no major distinctions between RANS and LES are noted around the blade for the two cases. Only the curves for MUR129 are showed in Fig. 10. Note that experimental measurements of the
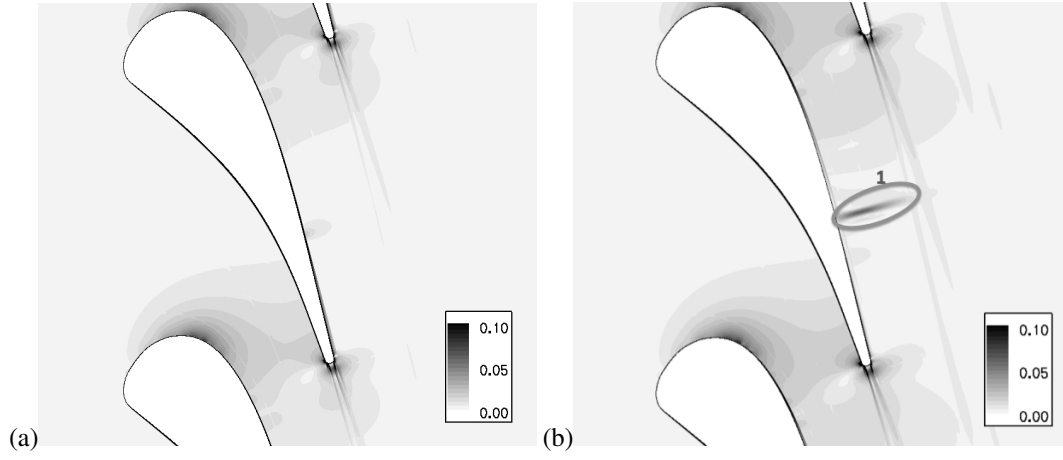
14

Figure 7: Mean RANS predictions of $||\frac{\partial \rho}{\partial x_i}||/\rho$ for (a) Case Ia and (b) Case Ib of Table 4.
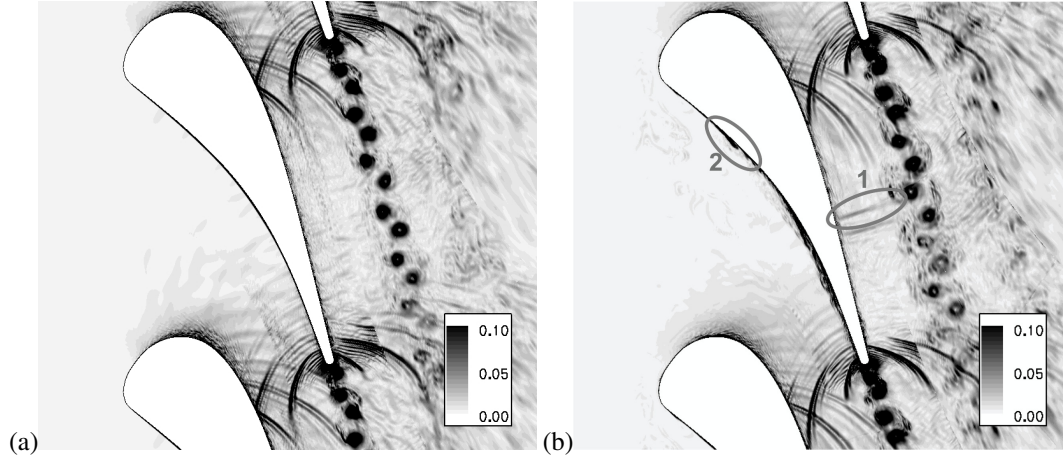

Figure 8: Instantaneous LES predictions of $||\frac{\partial \rho}{\partial x_i}||/\rho$ for (a) Case IIa and (b) Case IIb of Table 4.
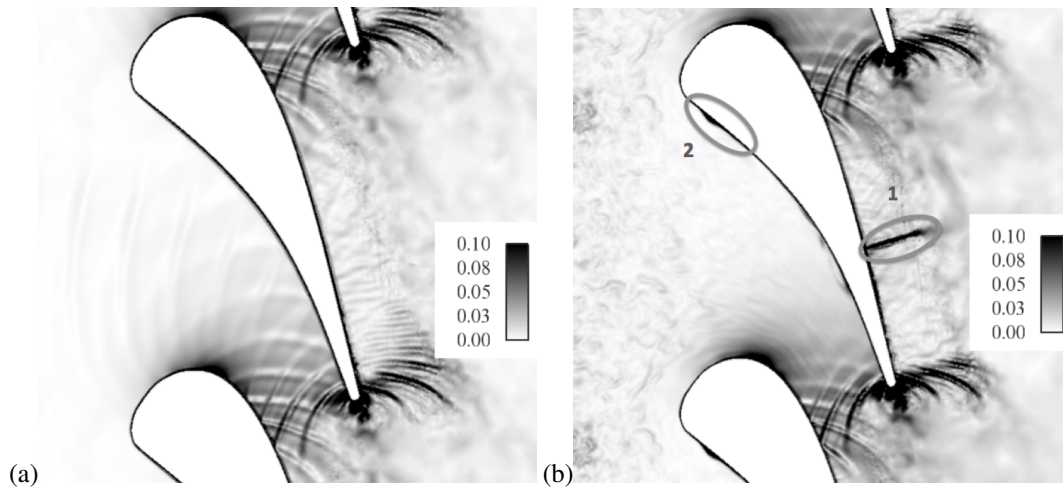

Figure 9: Instantaneous LES predictions of $||\frac{\partial \rho}{\partial x_i}||/\rho$ for (a) Case IIIa and (b) Case IIIb of Table 4.

15

isentropic Mach number are not available for the conditions of Table 1, the comparison presented serves only to gauge the magnitude of the parameter, $M_{is,2} \sim 0.84$ for all the numerical approaches vs $M_{is,2} \sim 0.88$ for the experimental data. As seen in Figs. 7 (a) & 8 (a) & 9 (a), the flow is subsonic all over the blade in MUR129. A more detailed investigation of the flow boundary layer behavior of the these two predictions is then carried out by looking at the heat transfer flux at the blade wall in Figs. 11 & 14.

(a)   (b)
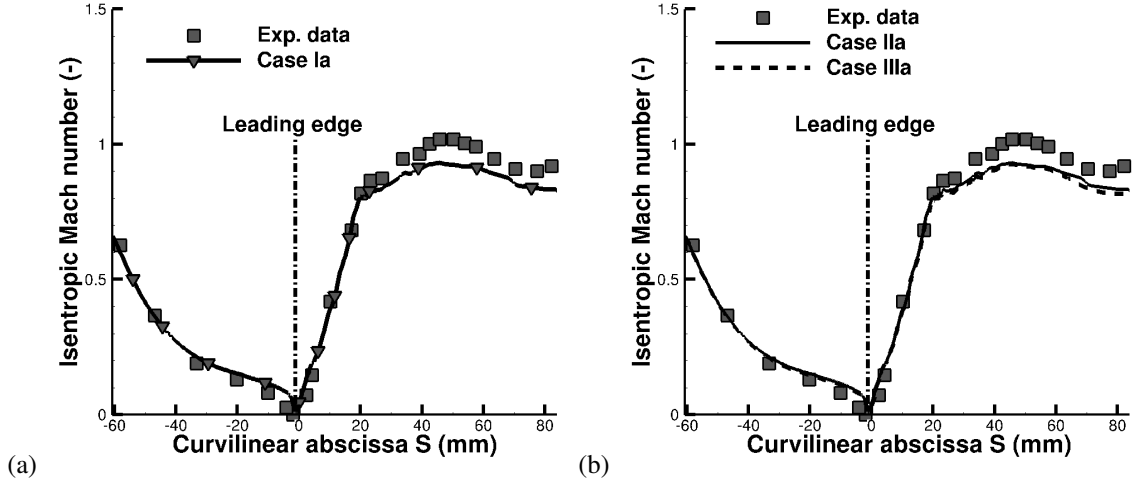
Figure 10: Isentropic Mach number distribution along the blade wall for (a) RANS and (b) LES computations of MUR129.

4.1.1. Test case wihout FST:

In MUR129, Fig. 11, the boundary layers remain mainly laminar on both suction and pressure sides. The heat transfer coefficient H obtained by RANS and LES is correctly estimated on the pressure side and on most of the suction side. The common behavior of H for RANS and LES in the near leading edge region corresponds to the development of the laminar boundary layer on both sides of the profile. RANS and LES anticipate the boundary layer transition seen on the experimental curve at $S = 75$ mm. This difference is common to RANS and LES in the estimation of heat transfer with respect to the experimental results, RANS and LES having nearly the same transition abscissa ($S \approx 61$mm). The disparity between experimental and numerical results is possibly due the pressure gradient, whose value for the solvers becomes negative at this specific location, as shown in Fig. 10, and eases transition at this spot for numerical predictions. The major difference between RANS and both LES is the level of heat transfer coefficient they reach after the transition, $H \approx 850$ W/m^2.K for RANS and $H \approx 500$ W/m^2.K for LES.

Based on this test case and although both approaches are theoretically very different, the flow is adequately captured by the steady and unsteady solvers confirming the proper behavior of the LES and RANS models for this operating condition which at the wall remains laminar and stationary. Views of the flow activity near the wall region and as captured by LES are shown on Fig. 12. For identification, the Q-criterion (colored by the velocity field) is
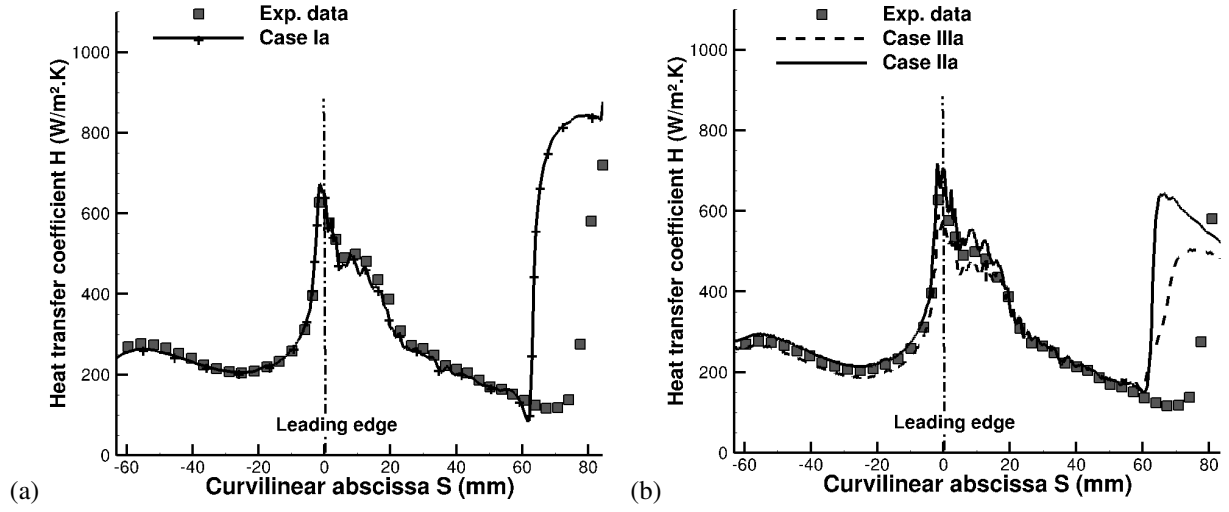
16

Figure 11: Heat transfer coefficient, H, predicted by (a) RANS and (b) structured and unstructured LES at MUR129.

employed to discriminate flow structures from pure shear at the wall. As evidenced by these results, limited flow activity is present on the pressure side, Fig. 12 (b), and almost no activity appears on the suction side. Very small vortices appear past the coordinates $S \approx 20$ mm where acoustic waves generated at the trailing edge upper blade impact the suction side of the blade placed below (Fig. 12 (a)). These structures however remain aligned and do not seem to initiate transition to a turbulent boundary layer.
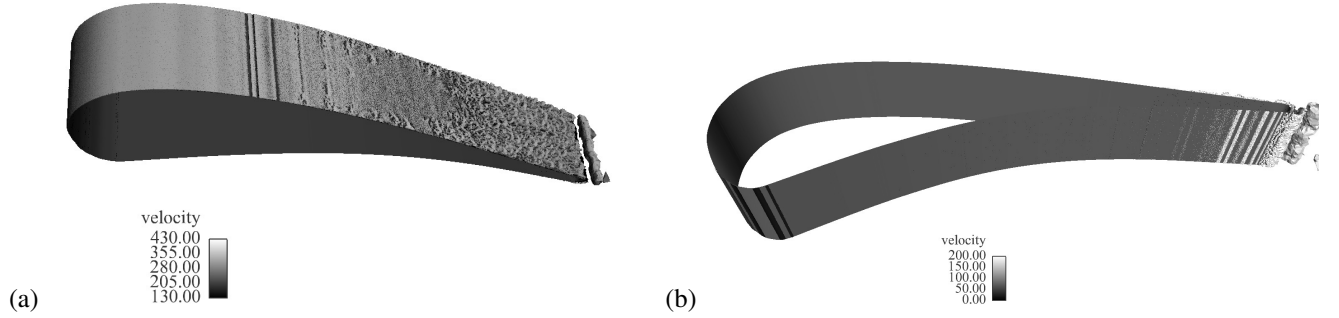

Figure 12: Instantaneous view of the LES flow activity on the (a) suction side and (b) pressure side of the MUR129 test case (Case IIIa of Table 4).

Similar observations hold for the pressure side of the blade where the activity is further delayed and only appears near the trailing edge. These observations are confirmed by the time/frequency maps, Fig. 13, constructed based on the temporal signal recorded for the three probes identified on Fig. 4 (b). Note that in this case, a Strouhal number

17

(based on the boundary layer hight and section bulk velocity) is used and time is adimensionalized accordingly. For all three points probed, low frequency and low intensity activity is visible confirming the pseudo stationary flow in this region also explaining the low level of the heat transfer coefficient around the blade.
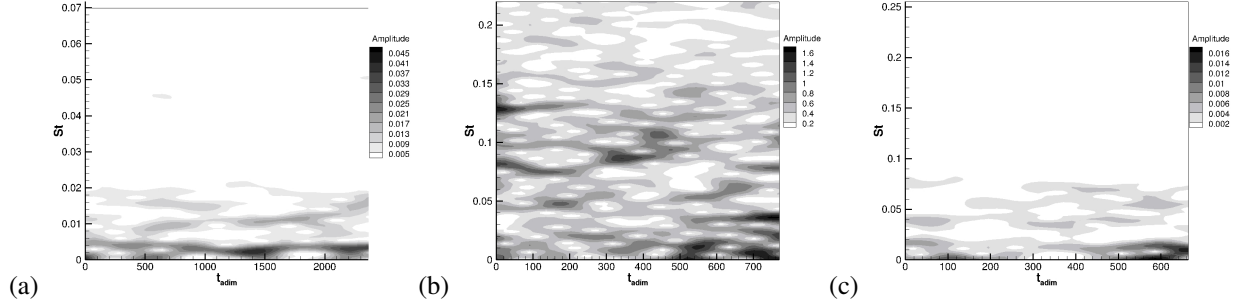

Figure 13: Temporal evolution of the frequency content recorded at the three probes identified on Fig. 4 (b): (a) Probe 1, (b) Probe 5 for the suction side of the blade and (c) Probe 9 for the pressure side.

4.1.2. Test case with FST:

Results of Fig. 14 (a) for MUR235, Table. 1, point to the difficulty for this flow and the importance of the main vein turbulence intensity on the boundary layer behavior. For this specific case and with the model adopted, RANS simulations fail to accurately predict the wall heat transfer on the pressure side. The heat transfer enhancement issued by the main flow turbulence is underestimated by about 30%; no influence of the FST is noticed on the pressure side: the heat transfer coefficient H is nearly identical to the MUR129 test case. In the leading edge zone, on the contrary, the γ-Re_θ model of Menter [43] is able to take into account the turbulence intensity effect. Further downstream on the suction side, RANS model does not correctly locate the experimental onset of pre-transition ($S \approx 20$ mm), which is triggered in the RANS simulation by the shock wave at $S \approx 62$ mm. At this location, the error reaches up to 70%. Indeed, RANS model predicts a decreasing evolution from $S \approx 20$ mm to $S \approx 62$ mm, whereas there is a plateau in the experimental heat transfer curve. For $S > 65$ mm, the MUR235 boundary layer is fully turbulent and RANS predicts the correct order of magnitude for the guide vane heating with a discrepancy of 30% if compared to the experimental results. For this case, the model seems better calibrated compared to the results obtained with the Abu-Ghannam approach and shown in Gourdain et al.[22].

Structured and unstructured LES predictions are also able to reproduce adequately the boundary layer heat transfer coefficient in the near leading edge region, Fig. 14 (b). In this zone, for both approaches the error is under the experimental uncertainty reported at 5%. The pressure side development improves if compared to RANS simulations. That is the heat transfer enhancement is captured by both solvers but the level of improvement is not sufficient to recover the experimental findings (18% error at most in Case IIIb and 10% in Case IIb). On the suction side, both LES strategies provide an improvement of the prediction when compared to RANS simulations especially for the
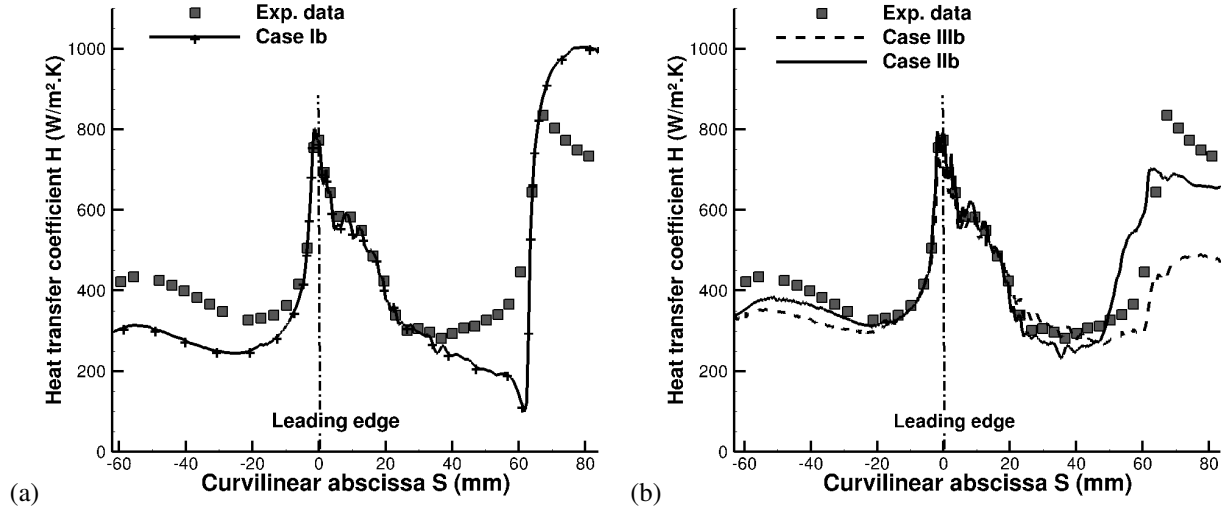
18

Figure 14: Heat transfer coefficient, H, predicted by (a) RANS and (b) structured and unstructured LES at MUR235.

prediction of the location and length of the onset of transition. Shock strengths are not equal indicating that both strategy differ and room for improvement still exists.
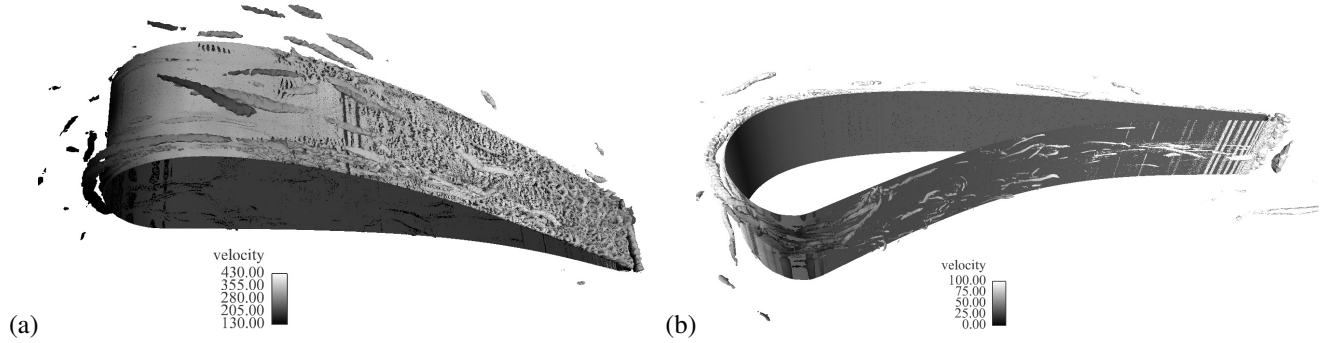

Figure 15: Instantaneous view of the LES flow activity on the (a) suction side and (b) pressure side of the MUR235 test case (Case IIIb of Table 4).

The main contribution of LES for this highly loaded blade profile naturally arises from the formalism ability to reproduce the proper boundary layer transition on the pressure side with increasing FST [8]. Although LES still underestimates the overall heat transfer on the pressure side, as noticed before, the difference with experimental data is reduced to 10% for the structured LES and 18% for the unstructured approach. The effect of FST is also clearly captured in this region of the flow, Fig. 14 (b). The main gain appears in the prediction of the pre-transition region of the suction side: *i.e.* from $S = 20$ mm to $S = 62$ mm. On this side of the blade and all around the leading edge, the heat transfer coefficient is estimated with an error less than 5% (*i.e.* within the experimental uncertainty) until $S = 50$ mm. The maximum error appears close to the trailing edge where structured and unstructured LES locally

19

underestimate the wall heat transfer by approximately 25% and 40%, respectively.

Visualizations of the flow instantaneous activity captured by LES are provided on Fig. 15. Compared to Fig. 12, flow structures are much stronger, much less aligned and initiated much earlier on the suction side, Fig. 15 (a), confirming the importance of such turbulence in the heat transfer enhancement in this region of the flow. On the pressure side, Fig. 15 (b), high disrupted flow structures are evidenced which are not present in the MUR129 case explaining the differences observed experimentally on the heat transfer coefficient. If investigating the time/frequency maps, Fig. 16, most of the differences between MUR129 and MUR235 occur at Probe 5, Fig. 16 (b), where a lot of intense activity appears. No clear pattern is however noted pointing to the turbulent nature of the activity present in this region of the flow.
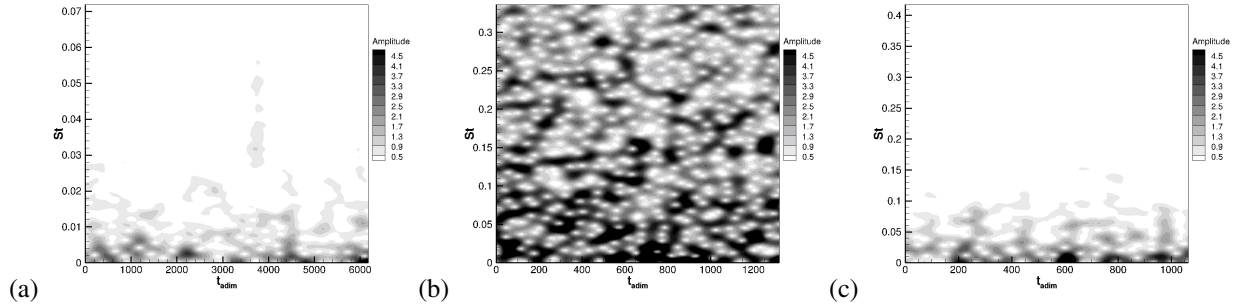

(a) (b) (c)

Figure 16: Temporal evolution of the frequency content recorded at the three probes identified on Fig. 4 (b): (a) Probe 1, (b) Probe 5 for the suction side of the blade and (c) Probe 9 for the pressure side.

More information illustrative of the blade boundary layer state along the blade can be found in Gourdain et al. [22].

4.2. LES sensitivity analysis and impact on the flow predictions

Although of interest and very promising, the previous LES set of predictions underline few aspects and difficulties specific to this approach. Both LES strategies used here clearly improve the flow predictions when compared to RANS simulations (at least over the set of modeling options retained for this work). In particular and with proper mesh design, structured or unstructured LES are able to correctly reproduce the FST sensitivity of this highly loaded turbine blade thereby improving heat transfer predictions along the blade wall. Details on the actual sensitivity of the approach seem therefore recommended in order to fully identify the potential sources of errors added by the multiple parameters introduced in a LES of such flows. Specific aspects of such a list are discussed below to highlight the potential of the two proposed approaches and the importance of known characteristic flow to resolved/grid scales.

4.2.1. Sensitivity of LES to mesh extent, topology and grid resolution

For the structured approach, the minimum cell size is less than 2μm all around the blade and in the wall normal direction (corresponding to a mean wall distance $y^+ \approx 1$). The wall normal expansion ratio used in this case is close

20

to 1.05. Note that experimentally the $2D$ nature of the flow is confirmed and the number of points in the span-wise direction needed for RANS simulation is found not to be a critical parameter and can be reduced to only 2 points. For structured LES such procedures are clearly not applicable due to the unsteady and $3D$ nature of the resolved turbulence needed for this approach. Figure 17 (a) presents the evolution of the normalized wall distances $\Delta x^+, \Delta y^+$ and Δz^+ around the blade: the maximum value of y^+ being always below 2. In other directions, normalized wall distances are kept under acceptable values ($< \Delta z^+ >= 25$ and $< \Delta x^+ >= 150$).
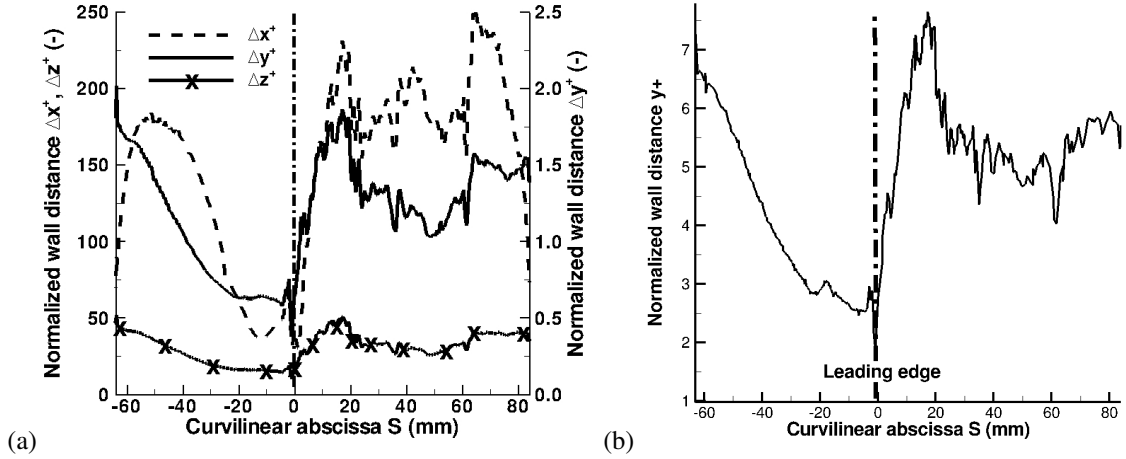

Figure 17: (a) Normalized wall distances Δx^+, Δy^+ and Δz^+ for the structured *elsA* code (Case IIb) and (b) normalized wall distances Δy^+ for the unstructured AVBP code (Case IIIb).

To achieve a mean wall distance of $y^+ \approx 4$ with the unstructured solver without impairing on the simulation time step (explicit solver), the minimum wall cell size needed is approximately $8\ \mu$m yielding $\Delta t \sim 1.54\ 10^{-8}$s for an acoustic CFL condition of 0.7. In the case of the structured solver, the scheme is implicit and the used acoustic CFL is much less drastic. For the current structured solver LES simulations, a CFL of 25 is used yielding a time step of $1.2\ 10^{-7}$s. The unstructured meshes rely on 5 layers of prismatic wall cells described in Subsection 3.3.1. The aspect ratio of the prisms is at maximum equal to 4 in the x and z directions resulting in $< \Delta z^+ >= 16$ and $< \Delta x^+ >= 16$ (Table. 2 recapitulates all these constraints). Figure 17 (b) presents the wall resolution issued by the unstructured mesh. As expected and by construction, the overall shape obtained on the unstructured mesh is in agreement with results of the structured mesh, Fig. 17 (a). Only the absolute value reached differs although they remain in a agreement with the imposed characteristic scales of the different cell topologies. This comforts the ability of LES to produce the proper gross behavior of the boundary layer of the MUR235 case with the proposed schemes and mesh constraints.

In the previous validation, only the cell characteristic size is addressed and this irrespectively of the extend in the span-wise direction of the computational domain. The computational domain dimensions are chosen to limit the dependency of the solution to the inlet/outlet positions as detailed in Subsection 3.3.1 and the span-wise extend of

the computational domain covers 10% of the vane span (*i.e.* 10 mm in the span-wise direction) in the previous set of results. Tests are introduced to better evaluate the dependency of the MUR235 results to this parameter, there include a 20% vane span simulation keeping the same set of numerical parameters: *i.e.* twice the total number of points for the structured solver and twice the number of cells for the unstructured solver and a 5% vane span simulation. Both test (20% and 5%) are compared to the baseline 10% vane span simulation for the structured and unstructured simulations (references Cases II&III) whose meshes are detailed in the first part of this Subsection and in Table 2 .
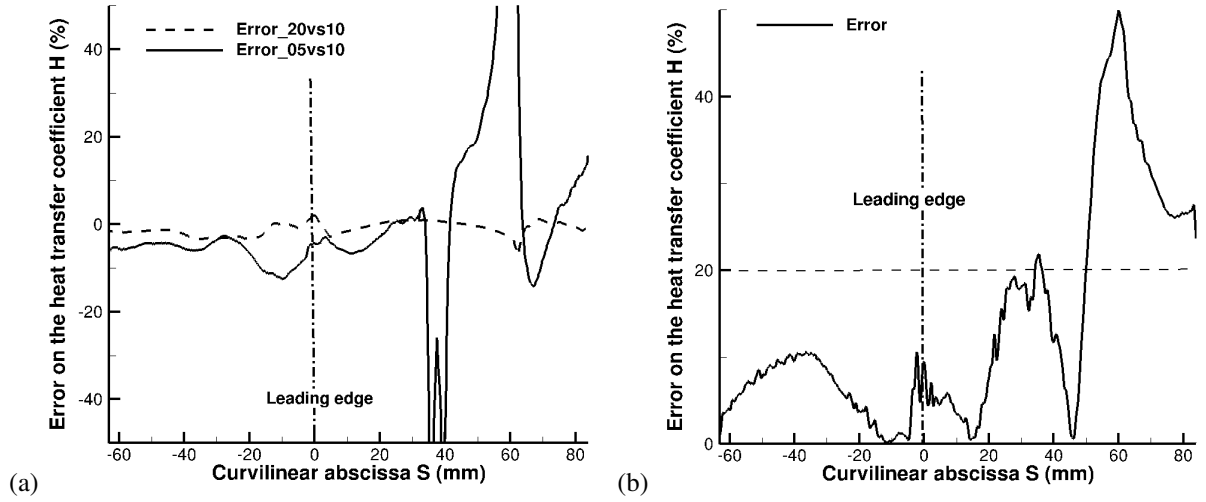

Figure 18: (a) Error on heat transfer coefficient, H when comparing a computation with 20% of the span to the baseline computation (10% of the span) and a computation with 5% to the baseline computation, for the structured solver and (b) Error on the H coefficient when confronting results from Case IIIb to Case IIb, both taking 10% of the span.

Results obtained with the fully structured meshes are provided on Fig. 18 (a) for the mean wall heat transfer and confirm that considering a 10% or 20% span-wise extent does not affect the predictions. The error remains below 5% for all curvilinear abscissae. The same conclusion is reached with the unstructured solver underlying that the numerics of both solvers (implicit versus explicit) with the dedicated resolutions are efficient for this test case. It also emphasizes the fact that flow structures and the turbulence developing from these two sets of simulations are not constrained by the span-wise extent of the computational domain. The same conclusion is not validated when comparing the case with the span-wise computational domain of 5 mm (Fig. 18 (a)). This span-wise extent is clearly insufficient to achieve a correct simulation. Turbulence is too constrained and errors on the heat transfer coefficient reach locally values above 100% (near the transition point). Note that a 10% span-wise length corroborates preliminary results obtained by LES on a fully structured solver by Bhaskaran et al. [8] using a 11 mm thick domain.

In Fig. 18 (b) a direct comparison is done between the results of the unstructured approach (Case IIIb) and the structured analysis (Case IIb) for MUR235. On the pressure side, the differences, taking as a reference the structured

solver, remain under 10% corroborating the analysis from Fig. 14 (b). The major discrepancy between the approaches is noticed after the pre-transition region, at $S = 62$ mm, when the transition is triggered. This difference could be explained by the shock capturing ability of the solvers and the SGS models behavior after the transition.

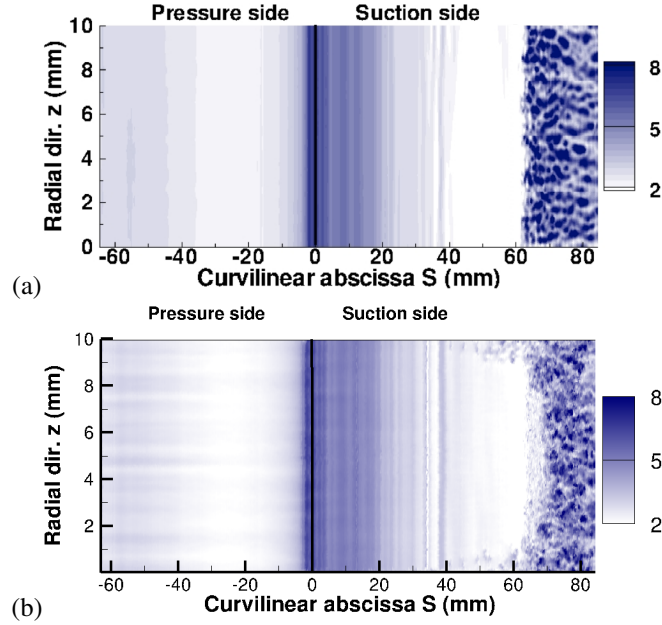### 4.2.2. Sensitivity of LES predictions to the FST

Figure 19: Instantaneous wall heat fluxes $Q(W/cm^2)$ (a) Case IIa and (b) Case IIIa.

Figures 19 & 21 show the instantaneous heat flux contours at the blade surface. The MUR129 test case ($Tu_0 = 1\%$, $Re_2 = 10^6$ and $M_{is,2} = 0.84$) is the simplest test case to simulate since the boundary layers remain mainly laminar on both suction and pressure sides. No turbulence is imposed at the inlet when comparing with experimental data at $Tu = 1\%$. As illustrated on Fig. 11, the heat transfer coefficient H is well captured by both solvers on the appropriate meshes. In experiments, the leading mechanism in this configuration is the natural boundary layer transition triggered by Tollmien-Schlichting waves. As seen on Fig. 19 (a) & (b), the instantaneous boundary layer visualizations of heat transfer show the uniformity of the flow in the span-wise direction and on both sides of the leading edge. At $S = 40$ mm, acoustic waves impact the blade suction side, Fig.8 (a) or Fig.9 (a), as a consequence local perturbations are visible at this location on Fig 19. These disturbances are, however, damped and it is the adverse pressure gradient at $S = 62$ mm which is responsible for the transition of the boundary layer. The two solvers show the same behavior for the MUR129 case.

The MUR235 ($Tu_0 = 6\%$, $Re_2 = 10^6$ and $M_{is,2} = 0.927$) test case although very close to MUR129 is much more complicated especially because of the near wall dynamics that are greatly affected by FST. The triggering mechanisms are here of twofolds: (a) FST which interacts with the local boundary layer state and (b) the shock-boundary layer
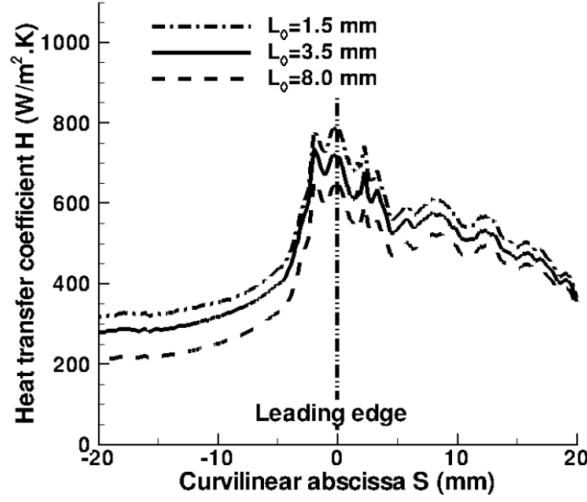
23

Figure 20: Effect of the inlet turbulent length scale L_0 on the wall heat transfer coefficient H predicted with (a) structured LES (Case IIb).

interaction on the suction side of the blade. Two parameters are needed to specify the turbulence injected at the inlet of the computation: Tu_0 and L_0. The data related to the FST intensity at the inlet has been measured in the experiments. However, no information on the turbulence length scale at the inlet is available. An exhaustive compilation of studies on the influence of Tu_0 and L_0 on the LS89 test case can be found in Liu [36].

In this particular analysis, to measure the influence of L_0, several simulations have been performed with both solvers for MUR235. Results obtained with the LES structured code are shown in Fig. 20 for L_0 = 1.5 mm, 3.5 mm and 8 mm. On the pressure side, the increase of L_0 is responsible for a decrease of 30% of the heat transfer coefficient. On the suction side, turbulence modifies the transition point position, S_{trans} = 55mm for L_0 = 1.5mm and S_{trans} = 60mm for L_0 = 8mm (out of Fig. 20). No influence is noted after the transition point. For the structured approach, the most energetic turbulent scale is finally chosen to meet the distance between parallel bars that generate turbulence in the experimental facility (1.5mm). For the unstructured approach, due to the different mesh discretization upstream of the blade, the L_0, which is responsible of the heat transfer coefficient plotted in Fig. 14 (b), is of 8mm. Ultimately, the flow topology has the same behavior leading to the results of Fig. 14 (b) and as shown in Figure 21, which presents similar views as in Fig. 19 for Cases IIb & IIIb (MUR235).

The turbulent eddies coming from the main upstream flow and imposed in the simulation by use of the synthetic turbulent injection model, Fig. 6, and Eq. (11), impact the leading edge of the blade, $S = 0$ mm. The future of these vortices from the leading edge around the blade involves first stretching of the initially isotropic structures and interactions with the local boundary layer flow. These complex interactions yield streaky structures originating from the stagnation flow region present at the leading edge and clearly visible on Fig. 21 in both LES's. This flow response explains the local heat transfer increase noticed previously for MUR235, differentiating it from MUR129. Note that

the relative size of the incoming turbulent structures to the local boundary layer thickness is probably of critical importance for a proper evaluation of the heat transfer rate along the blade (as already pointed out on Fig. 20).
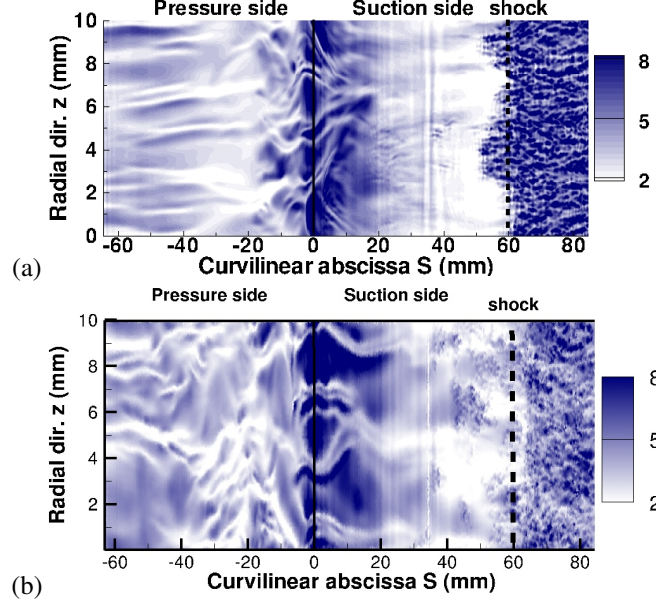

Figure 21: Instantaneous wall heat fluxes $Q(W/cm^2)$ computed with LES for MUR235 with (a) structured and (b) unstructured LES solvers.

On the suction side, $S > 0$, for both the structured and unstructured strategies, the vortices are rapidly distorted and eventually damped out by the accelerating flow issued by the strong curvature of the blade. At $S = 20$ mm, only elongated structures of span-wise size proportional to the incoming turbulent scales are present in both the structured and unstructured predictions. After this point, vortical stream-wise vortices eventually break-down and turbulent spots develop in the boundary layer (20 mm $< S <$ 50 mm) of the structured and unstructured solutions and as seen in White et al [62]. This wall behavior combined with the local adverse pressure gradient yields a slower decrease of the heat flux at the wall compared to MUR129 and it is only slightly prior to $S = 62$ mm (shock location) that a massively turbulent boundary layer appears. Although the overall dynamics is equivalent in the two LES's, subtle differences appear between the two predictions resulting in a slightly delayed transition point with the unstructured LES solver: the wall flow becomes fully turbulent slightly before the shock at $S = 55$ mm for the structured LES and at the shock for the unstructured LES method. A critical point underlined by such differences (aside from the proposed numerical approaches) is the dependency of such flow predictions to the characteristic length scale of FST [2] as already anticipated by Fig. 20.

On the pressure side, the initially generated flow structures appearing at the leading edge orient with the main flow stream-wise direction, mainly because of the favorable pressure gradient in this zone. Further down-stream, $S = -20$ mm, the local blade curvature may be at the origin of Görtler like vortices [55] and a clear rise of the wall

heat transfer is observed because of the perturbation of the thermal boundary layer in agreement with experimental findings. Observations apply for both the structured and unstructured LES's with similar conclusions as for the suction side.

5. Conclusion

This paper describes the investigations made about the prediction of wall heat transfer in a highly loaded turbine guide vane with RANS and two LES approaches (structured and unstructured). The effect of inlet turbulence on heat transfer and boundary layer development has been studied at two different flow operating conditions ($M_{is,2} = 0.840/0.927$, $Re_2 = 10^6$, $Tu_0 = 1/6\%$).

First, the result analyses show that the RANS approach (coupled with a transition criterion) is effective in predicting wall heat transfer when the boundary layer transition does not play a major role and it remains efficient in terms of computational resources. However, when the wall flow patterns depend on the main vein turbulence or from the inflow specification, RANS methods lack from predictive capability. The adoption of a transport equation for the transition criteria helps to partially overcome this problem although RANS model is still not capable of predicting the significant effect of turbulent structures when no transition is present.

Second, the study has revealed that LES can take into account the effects of FST in the wall region. Both structured and unstructured approaches are very promising methods, especially when an accurate description of the boundary layer transition is necessary. The simulated blade isentropic Mach number distribution and heat transfer coefficient show a very good agreement with the experiments of Arts et al. [6]. While LES still requires a very large computational power (a 30M points grid is necessary to represent only 10% of the vane span), this method is able to describe natural as well as by-passed transitions.

This work has also detected by two different approaches the presence of streaky structures on both blade sides and responsible for the intensification of heat transfer on the blade surface. Stretching of vortices from the inlet turbulence around the leading edge and the following transport of these vortices into the blade passage produce these boundary layer streaks. Around the leading edge, these streaks cause an increase of the laminar heat transfer. This phenomenon can also be observed on the pressure side. Note however that the suction side is less sensitive to inlet turbulence, if not due to the boundary layer transition. The present analysis also unveils the influence of the FST energetic length scale on the heat transfer coefficient.

Finally, this paper demonstrates that LES is ready to help the understanding of complex flow phenomena that are observed in high-pressure turbines (including at high Reynolds numbers). Unstructured LES, necessary to mesh intricate zones, demonstrates its ability to describe accurately the heat transfer in turbine backgrounds, even if this approach remains expensive in comparison with structured LES. An effort is nonetheless still necessary to use LES in an industrial context (full 3D, stage configurations, etc.) and sub-grid modeling could be improved to take into account the spatial distribution of the streaks near the wall [48].

References

[1] ABU-GHANNAM, B. & SHAW, R. 1980 Natural transition of boundary layers - the effects of turbulence, pressure gradient, and flow history. *J. of Mechanical Engineering Science* **22** (5), 213–228.

[2] ALFREDSSON, P.H. & MATSUBARA, M. 1996 Streaky structures in transition. In *Transitional Boundary Layers in Aeronautics* (ed. R.A.W.M Henkes & J.L. van Ingen), pp. 374–386. Royal Netherlands Academy of Arts and Sciences, Elsevier.

[3] AMAYA, J., COLLADO, E., CUENOT, B. & POINSOT, T. 2010 Coupling LES, radiation and structure in a gas turbine simulations. In *Proceedings of the Summer Program*, pp. 239–249.

[4] AMES, F. E. 1997 The influence of large-scale high-intensity turbulence on vane heat transfer. *J. Turbomachinery* **119**, 23–30.

[5] ANDERSON, D. A. 1984 *Computational Fluid Mechanics and Heat Transfer*. New York: Hemisphere Publishing Corporation.

[6] ARTS, T., DE ROUVROIT, M. LAMBERT & RUTHERFORD, A. W. 1990 Aero-thermal investigation of a highly loaded transonic turbine guide vane cascade. Technical Note 174. Von Karman Institute for Fluid Dynamics.

[7] BENARAFA, Y., CIONI, O., DUCROS, F. & SAGAUT, P. 2007 Temperature wall modelling for large-eddy simulation in a heated turbulent plane channel flow. *Int. J. Heat and Mass Transfer* **50** (21-22), 4360–4370.

[8] BHASKARAN., R. & LELE, S. 2010 Large eddy simulation of free-stream turbulence effects on heat transfer to a high-pressure turbine cascade. *J. Turbulence* **11** (6), 1–15.

[9] BOILEAU, M., STAFFELBACH, G., CUENOT, B., POINSOT, T. & BÉRAT, C. 2008 LES of an ignition sequence in a gas turbine engine. *Combust. Flame* **154** (1-2), 2–22.

[10] BOYLE, R. J. & AMERI, A.A. 1997 Grid orhogonality effects on turbine midspan heat transfer and performance. *J. Turbomachinery* **119** (1), 31–38.

[11] CABRIT, O. & NICOUD, F. 2008 DNS of a periodic channel flow with isothermal ablative wall. In *ERCOFTAC workshop - DLES 7*. Trieste, Italy.

[12] CAMBIER, L. & VEUILLOT, J.P. 2008 Status of the elsA CFD software for flow simulation and multidisciplinary applications. *46th AIAA Aerospace Science Meeting and Exhibit* (664).

[13] CELIK, I., SMIRNOV, A. & SMITH, J. 1999 Appropriate initial and boundary conditions for LES of a ship wake. In *Proceedings of the 3rd ASME/JSME Joint Fluids Engineering Conference*, , vol. FEDSM99-7851. San Francisco, California, USA.

[14] CHATELAIN, A. 2004 Simulation des grandes echelles d'ecoulements turbulents avec transferts de chaleur. Phd thesis, INP Grenoble.

[15] COLIN, O. & RUDGYARD, M. 2000 Development of high-order Taylor-Galerkin schemes for unsteady calculations. *J. Comput. Phys.* **162** (2), 338–371.

[16] DONÉA, J., ROIG, B. & HUERTA, A. 2000 High-order accurate time-stepping schemes for convection-diffusion problems. *Comput. Methods Appl. Mech. Eng.* **182**, 249–275.

[17] DUCHAINE, F., CORPRON, A., PONS, L., MOUREAU, V., NICOUD, F. & POINSOT, T. 2009 Development and assessment of a coupled strategy for conjugate heat transfer with large eddy simulation: Application to a cooled turbine blade. *Int. J. Heat Fluid Flow* **30**, 1129–1141.

[18] DUCROS, F., FERRAND, V., NICOUD, F., WEBER, C., DARRACQ, D., GACHERRIEU, C. & POINSOT, T. 1999 Large-eddy simulation of shock-turbulence interaction. *J. Comput. Phys.* **152**, 517–549.

[19] DULLENKOPF, K., SCHULZ, A. & WITTING, S. 1991 The effect of incident wake conditions on the mean heat transfer of an airfoil. *J. Turbomachinery* **113**, 412–418.

[20] FERZIGER, J. H. 1977 Large eddy simulations of turbulent flows. *AIAA J.* **15** (9), 1261–1267.

[21] FLORYAN, J. M. 1991 On the Görtler instability of boundary layers. *Progress in Aerospace Sciences* **28**, 235–271.

[22] GOURDAIN, N., GICQUEL, L.Y.M. & COLLADO, E. 2012 Comparison of RANS and LES for the prediction of the wall heat transfer in a highly loaded turbine guide vane. *AIAA J. Propulsion and Power* **28** (2).

[23] GUEZENNEC, N. & POINSOT, T. 2009 Acoustically nonreflecting and reflecting boundary conditions for vorticity injection in compressible solvers. *AIAA J.* **47**, 1709–1722.

[24] HAN, J. C., DUTTA, S. & EKKAD, S. V. 2000 *Gas Turbine Heat Transfer and Cooling Technology*. New York, NY, USA: Taylor & Francis.

[25] HIRSCH, C. 1990 *Numerical Computation of Internal and External Flows*, , vol. 2. New York: John Wiley & Sons.

[26] JAMESON, A. 1991 Time dependent calculations using multigrid, with applications to unsteady flows past airfoils and wings. *Tech. Rep.* AIAA-91-1596. AIAA 10th Computational Fluid Dynamics Conference.

[27] JAMESON, A., SCHMIDT, W. & TURKEL, E. 1981 Numerical solution of the Euler equations by finite volume methods using Runge-Kutta time stepping schemes. In *14th Fluid and Plasma Dynamic Conference* (ed. AIAA paper 81-1259). Palo Alto.

[28] JARRIN, N., BENHAMADOUCHE, S., LAURENCE, D. & PROSSER, R. 2006 A synthetic eddy method for generating inflow conditions for large eddy simulations. *Int. J. of Heat and Fluid Flow* **27**, (585–593).

[29] JIMÉNEZ, J. & MOIN, P. 1991 The minimal flow unit in near-wall turbulence. *J. Fluid Mechanics* **225**, 213–240.

[30] JOHNSON, M. W. 1994 A bypass transition model for boundary layers. *J. Turbomachinery* **116** (4), 759–764.

[31] KRAICHNAN, R. H. 1976 Eddy viscosity in two and three dimensions. *J. Atmos. Sci.* **33**, 1521–1536.

[32] KWON, O. J. & HAH, C. 1995 Simulation of three-dimensional turbulent flows on unstructured meshes. *AIAA J.* **33**.

[33] LAKSHMINARAYANA, B. 1996 *Fluid Dynamics and Heat Transfer of Turbomachinery*. New York, NY, USA: John Wiley & Sons, Inc.

[34] LAMARQUE, N. 2007 Schémas numériques et conditions limites pour la simulation aux grandes échelles de la combustion diphasique dans les foyers d'hélicoptère. Phd thesis, INP Toulouse.

[35] LÉONARD, T., DUCHAINE, F., GOURDAIN, N. & GICQUEL, L.Y.M. 2010 Steady/unsteady reynolds averaged navier-stokes and large eddy simulations of a turbine blade at high subsonic outlet mach number. In *Proceedings of the ASME TURBO EXPO 2010 Gas Turbine Technical Congress & Exposit*. Glasgow, UK.

[36] LIU, Y. 2007 Aerodynamics and heat transfer predictions in a highly loaded turbine blade. *Int. J. of Heat and Fluid Flow* **28**, 932–937.

[37] LUMLEY, J. L. 1978 Computational modeling of turbulent flows. *Adv. Appl. Mech.* **18**, 123–176.

[38] LUO, J. & LAKSHMINARAYANA, B. 1997 Numerical simulation of turbine blade boundary layer and heat transfer and assessment of turbulence models. *J. Turbomachinery* **119**, 794–801.

[39] MARTELLI, F., ADAMI, P. & BELARDINI, E. 2003 Heat transfer modelling in gas turbine stage. *Tech. Rep. ADA419187 University of Florence* .

[40] MAYLE, R. E. 1991 The role of laminar-turbulent transition in gas turbine engines. *J. Turbomachinery* **113**, 509–537.

[41] MENDEZ, S. & NICOUD, F. 2008 Large-eddy simulation of a bi-periodic turbulent flow with effusion. *J. Fluid Mechanics* **598**, 27–65.

[42] MENTER, F.R. 1994 Two-equation eddy viscosity turbulence model for engineering applications. *AIAA J.* **32** (8).

[43] MENTER, F.R., LANGTRY, R.B., LIKKI, S.R. & SUZEN, Y.B. 2006 A correlation-based transition model using local variables - Part 1: model formulation. *J. Turbomachinery* **128** (3).

[44] MICHELASSI, V., WISSINK, J. & RODI, W. 2002 Analysis of DNS and LES of flow in a low pressure turbine cascade with incoming wakes and comparison with experiments. *Flow, Turbulence and Combustion* **69**, 295–330.

[45] MOIN, P. 2002 Advances in large eddy simulation methodology for complex flows. *Int. J. of Heat and Fluid Flow* **23** (5), 710–720.

[46] MOIN, P., SQUIRES, K. D., CABOT, W. & LEE, S. 1991 A dynamic subgrid-scale model for compressible turbulence and scalar transport. *Phys. Fluids* **A 3** (11), 2746–2757.

[47] NICOUD, F. & DUCROS, F. 1999 Subgrid-scale stress modelling based on the square of the velocity gradient. *Flow, Turb. and Combustion*

62 (3), 183–200.

[48] NICOUD, F., H, BAYA TODA., CABRIT, O., S., BOSE & LEE, J. 2011 Using singular values to build a subgrid-scale model for large eddy simulations. *Phys. Fluids* **23** (8).

[49] PASSOT, T. & POUQUET, A. 1987 Numerical simulation of compressible homogeneous flows in the turbulent regime. *J. Fluid Mechanics* **181**, 441–466.

[50] POINSOT, T. & VEYNANTE, D. 2005 *Theoretical and Numerical Combustion*. R.T. Edwards, 2nd edition.

[51] POPE, S. B. 1983 Consistent modeling of scalar in turbulent flows. *Phys. Fluids* **2**, 404–408.

[52] POPE, S. B. 2000 *Turbulent flows*. Cambridge University Press.

[53] SAGAUT, P. 2000 *Large Eddy Simulation for incompressible flows*. Springer-Verlag.

[54] SAGAUT, P. & DECK, S. 2009 Large-eddy simulation for aeronadymics: status and perspectives. *Phil. Trans. R. Soc. Lond.* **367**, 2849–2860.

[55] SARIC, W. S. 1994 Görtler vortices. *Ann. Rev. Fluid Mech.* **26**, 379–409.

[56] SCHØNFELD, T. & RUDGYARD, M. 1999 Steady and unsteady flows simulations using the hybrid flow solver AVBP. *AIAA J.* **37** (11), 1378–1385.

[57] SMAGORINSKY, J. 1963 General circulation experiments with the primitive equations: 1. the basic experiment. *Mon. Weather Rev.* **91**, 99–164.

[58] SMIRNOV, E. & SMIRNOVSKY, A. 2009 Turbine vane cascade heat transfer predictions using a modified version of the $Re_{\theta t}$ laminar-turbulent transition model. *Int. Symp. On Heat Transfer in Gas Turbine Systems* .

[59] STAFFELBACH, G., GICQUEL, L.Y.M., BOUDIER, G. & POINSOT, T. 2009 Large eddy simulation of self-excited azimuthal modes in annular combustors. *Proc. Combust. Inst.* **32**, 2909–2916.

[60] SUZEN, Y.B. & HUANG, P.G. 2000 Modeling of flow transition using an intermittency transport equation. *J. Fluids Eng.* **122**, 273–284.

[61] TENNEKES, H. & LUMLEY, J. L. 1972 *A first course in turbulence*. Cambridge: M.I.T. Press.

[62] WHITE, F. M. 1991 *Viscous fluid flow*. New-York: McGraw-Hill.

[63] WILCOX, D.C. 1988 Reassessment of the scale-determining equation for advanced turbulence models. *AIAA J.* **26**, 1299–1310.

[64] WISSINK, J. & RODI, W. 2006 Direct numerical simulation of flow and heat transfer in a turbine cascade with incoming wakes. *J. Fluid Mechanics* **569**, 209–247.

[65] XIONG, Z. & LELE, S.K. 2007 Stagnation-point flow under free-stream turbulence. *J. Fluid Mechanics* **519**, 201–232.

[66] YARDI, N. R. & SUKHATME, S. P 1978 Effect of turbulence intensity and integral scale of a turbulent free stream on forced convection heat transfer from a circular cylinder in cross-flow. *6th International Heat Transfer Conference.* **5**, 347–352.

[67] YOON, S. & JAMESON, A. 1987 An LU-SSOR scheme for the Euler and Navier-Stokes equations. *25th AIAA Aerospace Science Meeting* .

[68] ZHONG, B. & TUCKER, P.G. 2005 LES and hybrid LES/RANS simulations for conjugate heat transfer over a matrix of cubes. In *In 43rdh AIAA Aerospace Sciences Meeting and Exhibit*.